Solid-State Batteries

International Edition: DOI: 10.1002/anie.201910993
German Edition: DOI: 10.1002/ange.201910993

Anisotropically Electrochemical–Mechanical Evolution in Solid-State Batteries and Interfacial Tailored Strategy

Nan Sun, Qingsong Liu, Yi Cao, Shuaifeng Lou, Mingyuan Ge, Xianghui Xiao, Wah-Keat Lee, Yunzhi Gao, Geping Yin, Jiajun Wang, and Xueliang Sun**

Abstract: *All-solid-state batteries have attracted attention owing to the potential high energy density and safety; however, little success has been made on practical applications of solid-state batteries, which is largely attributed to the solid–solid interface issues. A fundamental elucidation of electrode–electrolyte interface behaviors is of crucial significance but has proven difficult. The interfacial resistance and capacity fading issues in a solid-state battery were probed, revealing a heterogeneous phase transition evolution at solid–solid interfaces. The strain-induced interfacial change and the contact loss, as well as a dense metallic surface phase, deteriorate the electrochemical reaction in solid-state batteries. Furthermore, the in situ growth of electrolytes on secondary particles is proposed to fabricate robust solid–solid interface. Our study enlightens new insights into the mechanism behind solid–solid interfacial reaction for optimizing advanced solid-state batteries.*

Introduction

Taking advantage of high energy density and long lifetime, lithium-ion batteries (LIBs) have powered portable electronic devices for decades.[1] The demand for LIBs in electric vehicles and grid-scale energy storage applications raise increasing safety concerns that are associated with widely used highly flammable organic electrolyte.[2] Instead of the liquid electrolytes, solid-state electrolytes that utilize non-flammable inorganic materials have received tremendous attention.[3] In the search for appropriate solid-state electrolytes, intensive research efforts have devoted to developing highly ionic conductive solid-state electrolytes including the sulfides, oxides, and polymers.[4] Ion conductivity, one of the key physical properties, has undergone significant improvement in recent years.[5]

Despite these significant advances in improving ionic conductivity, the electrochemical performance of most solid-state batteries is still unsatisfactory, which is generally ascribed to a number of interfacial issues, such as high interfacial resistance, chemical incompatibility, and low interfacial stability.[3,6] Poor physical contact and heterogeneous contact points may lead to uneven potential distribution at solid–solid interfaces, which are detrimental for lithium-ion transport and rate performance.[7] The volume expansion and shrinkage of battery materials upon electrochemical cycling may further cause contact loss with solid-state electrolytes and deteriorate capacity retention.[8] In addition, an interfacial chemical reaction may also contribute to high interfacial resistance and low cycling stability.[9] As a general solution, interfacial modification with a variety of functional materials may suppress interfacial chemical reaction and improve interfacial compatibility, but make few contributions to mitigate poor physical contact.[10] As a result, engineering better interfaces to improve physical contact and chemical compatibility simultaneously is critical for solid-state batteries but has proven difficult in part because the experimental evaluation of the solid–solid interface remains challenging and exact mechanism associated with high interfacial resistance has not been ascertained precisely.

The present work aims to present a visualized study of microstructural evolution of active battery particles in sulfide solid-state batteries and elucidate the interfacial resistance in the solid–solid point contact mechanism. To avoid space-charge layer effect in sulfide solid-state electrolyte, transition metal sulfides have been extensively employed as electrode materials.[11] FeS_2, in particular, is a promising candidate as it is inexpensive, environmentally benign, and energy-dense. Also, taking advantage of the four-electron conversion reaction, FeS_2 can provide a high theoretical capacity of 894 $mAh\,g^{-1}$. As a result, FeS_2 was selected as a model material and assembled with $Li_7P_3S_{11}$ in a solid-state battery. With the combination of electrochemistry and operando synchrotron X-ray nanotomography, we disclose the origin of low reversibility capacity of solid-state batteries and reveal a heterogeneous phase conversion of FeS_2 along with solid-solid contact interface. Further, large volume expansion of FeS_2 and the resulting contact loss with sulfide electrolytes also deteriorate the electrochemical reaction in solid-state batteries. In light of the performance degradation mechanism,

[*] N. Sun, Q. Liu, Y. Cao, S. Lou, Prof. Y. Gao, Prof. G. Yin, Prof. J. Wang
MIIT Key Laboratory of Critical Materials Technology for New Energy Conversion and Storage, School of Chemistry and Chemical Engineering, Harbin Institute of Technology
Harbin 150001 (China)
E-mail: jiajunhit@hit.edu.cn
M. Ge, X. Xiao, W. Lee
National Synchrotron Light Source II
Brookhaven National Laboratory
Building 743 Ring Road, Upton, NY 11973 (USA)
Prof. X. Sun
Department of Mechanical and Materials Engineering
University of Western Ontario
1151 Richmond St, London, Ontario, N6A 3K7 (Canada)
E-mail: xsun9@uwo.ca
Supporting information and the ORCID identification number(s) for the author(s) of this article can be found under: https://doi.org/10.1002/anie.201910993.

we proposed a strategy via in situ syntheses of sulfide electrolytes into secondary-particle FeS_2 to fabricate robust and homogeneous solid–solid interface. The firmly anchored point–point interface not only improves the interfacial wettability but also buffers volume strain to inhibit solid–solid interface loss. Our observation gives new insights into the interface resistance mechanism in solid-state batteries and demonstrate the importance of in situ growth strategies to preserve the interfacial integrity for solid-state batteries.

Results and Discussion

Physical Characterizations

The Li^+ superionic $Li_7P_3S_{11}$ (LPS) synthesized by a simple liquid-state reaction exhibits a triclinic structure with a space group of $P-1$, as shown in Figure 1 A. All Li sites are fully occupied and P/S atoms make individual PS_4 tetrahedra or P_2S_7 ditetrahedra. The primary cell has two formula units with seven symmetrically distinct lithium sites.[12] Figure 1 B shows the X-ray diffraction for the commercial FeS_2, glass-ceramic $Li_7P_3S_{11}$ solid electrolyte, and $FeS_2 + LPS + C$ composite anode material. The commercial FeS_2 exhibits a cubic phase (space group $Pa-3$), and the crystal structure of pyrite FeS_2 is shown in the Supporting Information, Figure S2 A.[13] The characteristic peaks of the $Li_7P_3S_{11}$ can be assigned to the (102), (−212), (−1−21), and (113) planes, which confirm that $Li_7P_3S_{11}$ was obtained without any impurities (Supporting Information, Figure S1).[14] The characteristic peaks of $Li_7P_3S_{11}$ and FeS_2 can be found clearly in the XRD pattern of the composite anode material that indicates the solid electrolyte mixed with the active material successfully. Furthermore, the morphologies and microstructures of the FeS_2, $Li_7P_3S_{11}$ and composites anode material were observed by SEM (Supporting Information, Figure S2 B–D).

Surface analysis of the $Li_7P_3S_{11}$ solid electrolyte was performed by XPS, and the spectra of the S 2p and P 2p signals are denoted in Figure 1 C. The S 2p signal is assigned to three different spin–orbit split signals, which are bridging (P–S–P, 163 eV), double bound (P=S, 162.1 eV), and single bond (P–S–Li, 161.5 eV) sulfur atoms. The P 2p signal can be described by two different species corresponding to $P_2S_7^{4-}$ and PS_4^{3-} species, respectively.[12,15] The chemical information observed in these XPS spectra is well consistent with previous reports.[12,15] The Raman spectra in Figure 1 D was further used to characterize the chemical species in the samples. The stretching of PS_4^{3-} (*ortho*-thiophosphate) and $P_2S_7^{4-}$ (pyro-thiophosphate) anions are observed at the peaks around 420 cm^{-1} and 405 cm^{-1}.[16] The peaks at 340 cm^{-1} 340 cm^{-1} can be attributed to the FeS_2.[17] The characteristic peaks of LPS and FeS_2 appear simultaneously in the composite. In the FTIR spectrum (Supporting Information, Figure S3), characteristic absorption peaks of LPS and FeS_2 appear simultaneously in the composite. These results indicate that the electrolyte and the active material are well mixed in the composite.

The Li-ion conductivity and activation energy were determined by temperature-dependent electrochemical impedance spectroscopy, as shown in Figure 1 E. Arrhenius plot shows a temperature-dependency for ionic conductivity (Figure 1 F). The calculated activation energy and room-temperature ionic conductivity are 9.493 KJ mol^{-1} and 1.27×10^{-4} S cm^{-1}, respectively.

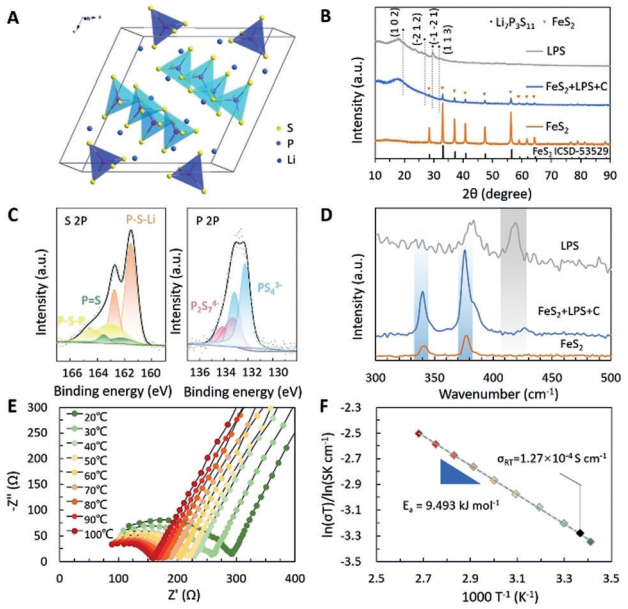

Figure 1. Physical characterizations. A) Crystal structure of triclinic $Li_7P_3S_{11}$. B) X-ray diffraction patterns of the neat $Li_7P_3S_{11}$ electrolytes, commercial FeS_2, and electrode composites. C) XPS spectra of P and S for $Li_7P_3S_{11}$. D) The Raman spectra of the neat $Li_7P_3S_{11}$ electrolytes, commercial FeS_2, and electrode composites. E) Nyquist plot of spectra between 20 °C and 100 °C. F) Arrhenius plot of Li^+ diffusivity of $Li_7P_3S_{11}$.

Low Coulombic Efficiency and Large Voltage Hysteresis in All-Solid-State Batteries

To gain insight into how a solid-state electrolyte affects electrochemical performance, a solid-state battery was assembled. The first cycle is of particular importance, as the electrochemical behavior in solid-state batteries may be distinctive from conventional liquid electrolyte-based batteries. Indeed, the discharge curve in Figure 2 A shows only one plateau around 1.5 V in this solid-state battery for the initial cycle without obvious electrolyte decomposition at low potentials. In sharp contrast, apart from the voltage plateau at 1.5 V, an additional reaction occurring below 1.0 V at the liquid state battery which can be attributed to solid electrolyte interphase (SEI) formation in conventional carbonate liquid electrolyte (Figure 2 B).[18] The absence of obvious SEI formation and the less electrolyte decomposition can offer more advantages for solid-state batteries. Despite this merit, the voltage hysteresis between charge and discharge process is nearly twice larger in solid-state batteries (0.51 V) than liquid batteries (0.26 V), and the coulombic efficiency of the FeS_2-sulfide solid-state battery is also low (54.77 %), which could be attributed to the formed high ionic transport resistance at the initial cycle. To understand this phenomenon, the electrochemical resistance after 1st and 2nd discharge was

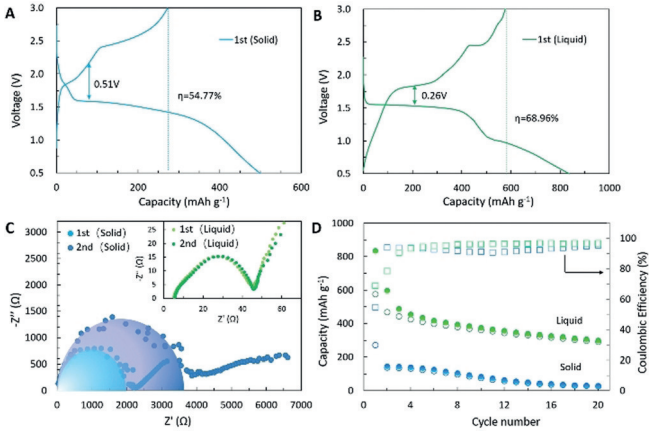

Figure 2. Low coulombic efficiency and large voltage hysteresis in all-solid-state batteries. A) The initial discharge and charge profiles of the solid-state batteries. B) The initial discharge and charge profiles of the conventional liquid coin batteries. C) Impedance spectra after 1st and 2nd discharge in solid-state batteries. Inset: corresponding impedance spectra in liquid batteries. D) Capacity retention comparison of batteries.

monitored with impedance spectroscopy in the Li/ $Li_7P_3S_{11}$/ FeS_2 solid-state battery to correlate to the observed large voltage hysteresis and low cycle efficiency, as depicted in Figure 2C. A significant increase in interfacial resistance was clearly observed in solid-state batteries, while negligent change occurs at liquid electrolyte batteries (as shown in the inset).

The ionic conductivity loss and poor coulombic efficiency in solid-state batteries could be due to the issues associated with the solid–solid interface, where the volume change of FeS_2 upon lithium insertion may result in the contact loss of the FeS_2 phases with the solid electrolyte or the conductive carbon network making subsequent electrochemical reaction difficult, resulting in little reversible capacity was achieved in the subsequent cycles (Figure 2D). The details of the charge and discharge profiles are shown in the Supporting Information, Figure S4.

By comparing the CV curves of the first three cycles of the solid-state battery and the liquid battery (Supporting Information, Figures S5A,B). In the solid-state battery, there is almost no obvious redox peak in the solid-state battery except for a reduction peak in the first discharge process. It is indicated that the electrochemical reaction is too slow due to the large interfacial resistance formed by the first lithiation. In contrast, the CV curve of the liquid battery exhibits good reversibility, so the capacity of the liquid battery is high, and the stable interface in the liquid battery further benefits.

Heterogeneous Phase Conversion

The increasing electrochemical impedance may suggest an electrochemically induced contact loss at the interface between the solid electrolyte and the active battery particles. To further understand this phenomenon, the $Li_7P_3S_{11}/FeS_2$ interface was quantified with operando synchrotron X-ray nanotomography.[19] We have previously applied this unique approach to characterizing lithium-ion battery electrodes.[20] Owing to the distinctive attenuation coefficients in elements with different depth of discharge (DOD), FeS_2 compositions with high X-ray absorption at the energy of iron K-edge are easily distinguished from light-element including $Li_7P_3S_{11}$ electrolyte. Further to morphology and element identification, high-resolution chemical information can also be obtained with the TXM-XANES approach by tuning hard X-ray energy across Fe K-edge. Herein, to investigate the chemical homogeneity and phase distribution in real 3D in FeS_2 particles, we performed in situ 3D XANES (or called spectroscopy tomography) measurement to track phase evolution in sulfide solid-state electrolytes (Figure 3A). The

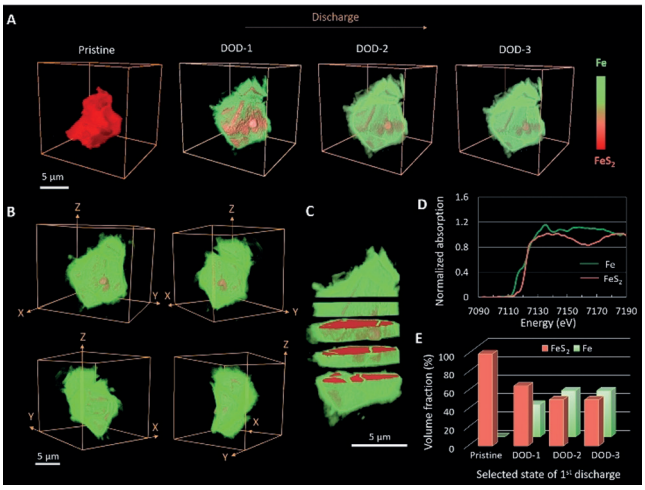

Figure 3. Operando X-ray spectroscopic nanotomography. A) Phase distribution as a function of discharging states. B) Discharged FeS_2 at DOD-3 from different orientations. C) Cut-view of FeS_2 at lithiated state. D) The XANES spectra of standard FeS_2 and Fe. E) Phase volume fraction obtained from 3D quantitative analysis.

chemical maps were generated by the linear combination fitting with the XANES spectra of the standard phases (Figure 3D), and the color legend illustrated in Figure 3A, where red and green represent FeS_2, and Fe phases, respectively. As for a conventional conversion reaction in batteries, phase conversion usually starts from progressive nucleation and followed by homogeneous propagation from the surface of a particle until the particle core is fully converted.[21] Nevertheless, practical conditions in solid-state batteries are complex and homogeneous phase conversion in the solid–solid interface has proven difficult. Any changes on the solid–solid interface and the resulting contact loss may cause heterogeneous phase conversion. We first observe the converted Fe phase front appear and progressively penetrate into the particle, transforming the pristine FeS_2 phase and resulting in large volume expansion/cracks. However, the subsequent phase propagation seems to slow down and the phase transformation nearly terminates at low discharging potentials. To take a closer view, snapshots for the reconstructed tomography for the discharged FeS_2 at DOD-3 from different orientations are shown in Figure 3B and the associated cut-

view is provided in Figure 3C, suggesting the core–shell model at the finial discharging state. To quantify the phase evolution, the segmentation of 3D-sub-volume of the particle at different states of discharge and the quantitative analysis is shown in Figure 3E, further indicating the termination of the conversion reaction at the low potentials in solid-state batteries.

Apart from the 3D view, the propagation of the reaction front is also visualized by the 2D cross-section mapping along with different orientations (*X-Y*, *Y-Z*, *X-Z*) shown in Figure 4A. Basically, a core–shell model can be clearly observed

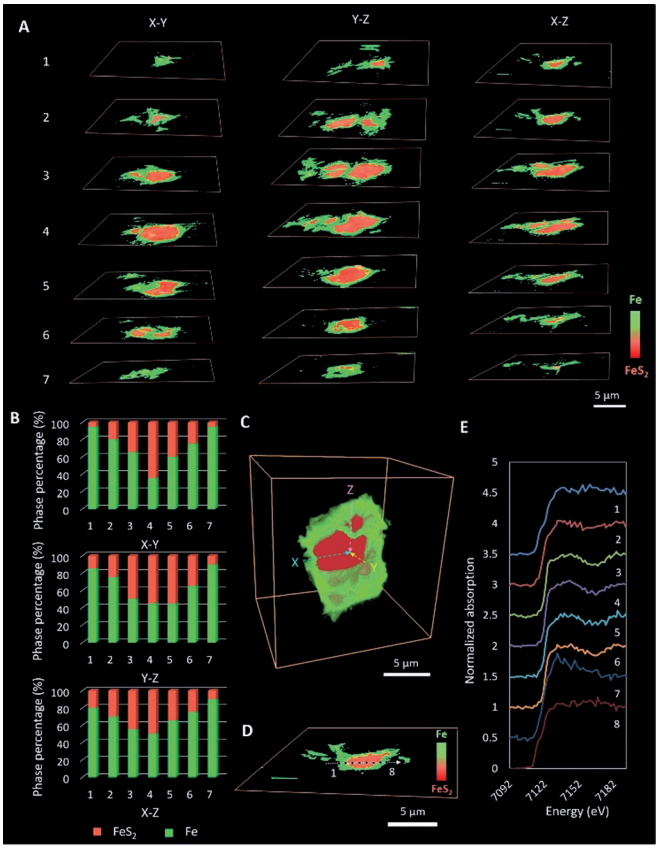

Figure 4. 2D cross-section mapping and heterogeneous phase conversion. A) Cross-sectional slides along *X-Y*, *Y-Z*, and *X-Z* planes. B) Phase composition analysis of selected slides from different orientations. C) The internal microstructure of the same particle with a cut-away view. D) Chemical phase mappings of the selected cross-section slide. E) Line profile of XANES spectra along the horizontal axis at the selected cross-section slide.

in most cross-section images. Taking a close look at the slides at the top and bottom in which they are near to the particle surface, Fe phase dominates the major component at slice 1 and 7 along the *X-Y* plane. In contrast, two phases of FeS_2 and Fe co-exist across the particle along the *Y-Z* and *X-Z* plane (also see the histogram of phase composition shown in Figure 4B). This phenomenon indicates the phase transformation seems to be heterogeneous along different orientations, and the phase front prefers to occurring along the *X-Y* plane which may be attributed to more electronic–ionic accessible sites along this plane. To further understand the orientation-dependent phase transformation, we generate a 3D phase composition distance maps as a function of depth from the particle surface at the final discharged state (Figure 4C), and the statistics profile is shown in the Supporting Information, Figure S6. The profile indicates that phase boundaries prefer to propagating into the bulk along the *Z* axis as the electrochemical reaction proceeds. From the line-scanning analysis at the selected slice (Figure 4D,E; Supporting Information, Figure S7), the asymmetric energy shift for iron K-edge and the different propagation thickness also suggests a unidirectional reaction for the phase conversion of FeS_2 in solid-state batteries.

For comparison, lithiation behavior of FeS_2 in the conventional liquid electrolyte was also investigated by in situ 2D TXM, as shown in the Supporting Information, Figure S8. A nearly uniform conversion reaction with a continuous expansion of the particles as well as crack initiation and growth were observed in conventional liquid electrolyte batteries.[22] Quantitative analysis of the microstructural changes during the first discharge is shown in the Supporting Information, Figure S9. As the phase propagates and cracks appear, the liquid electrolyte can easily permeate into these cracks to fill the void/cracks and access the surface of active battery particles, therefore the electrochemical reaction further proceeds and phase boundaries front can move smoothly. An illustration (Supporting Information, Scheme S1) clearly interprets the difference in electrochemical reactions between solid-state and liquid-electrolyte-based batteries.

Interfacial Resistance Mechanism and Physical Contact Loss

Here, in situ EIS of the first two cycles were performed to gain a detailed understanding of the interfacial resistance mechanism in solid-state batteries (Supporting Information, Figures S10, S11). The initial discharge cycle is shown in Figure 5A and the evolution of the impedance spectra at the different DOD are illustrated in Figure 5B.[23] To improve understanding the evolving interfacial resistance mechanism in solid-state battery electrode, a series of solid-state batteries

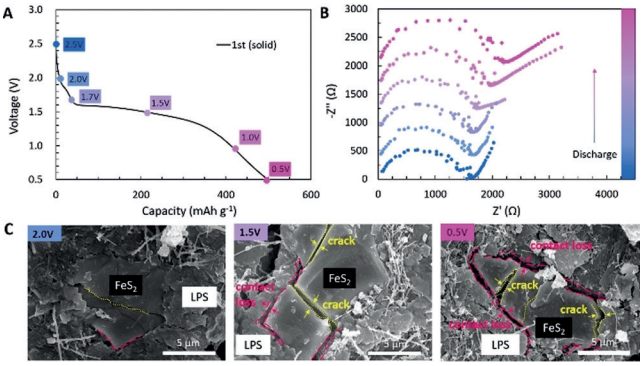

Figure 5. Interfacial resistance mechanism and physical contact loss in solid-state batteries. A) First cycle discharge profile of the solid-state cell. B) Impedance spectra recorded during the discharge period. C) Scanning electron micrographs of the electrode composite of FeS_2 and $Li_7P_3S_{11}$ at the first discharge in solid-state batteries.

at different discharging states were dissembled and the morphologies of FeS_2 composite electrodes were investigated with SEM (Figure 5C). As for the DOD-2V electrode, FeS_2 active particles are firmly embedded in the composite and most edges of FeS_2 particles contact the solid-state electrolyte intimately. As the discharging process proceeds, volume expansion of FeS_2 particles occurs and the active FeS_2 particles begin to separate from the solid-state electrolyte. It is well-known that most conversion materials undergo huge volume expansion upon lithium-ion insertion, which is responsible for the contact loss between FeS_2 and solid-state electrolytes.[7b,10] Meanwhile, the heterogeneous phase transformation from different orientations also results in the sum of the axial strains within the FeS_2 particles, which further deteriorate the contact loss. We, therefore, suggest that large volume expansion in combination with the heterogeneous axial strain provokes the contact loss between FeS_2 and solid-state electrolytes at the initial electrochemical cycle. Unlike liquid electrolyte which can flow and penetrate into the cracks or pores in the electrode, solid-state electrolytes cannot easily fill into the emerging gap once continuous ionic/electronic contact loss occurs and the capacity fading is inevitable.

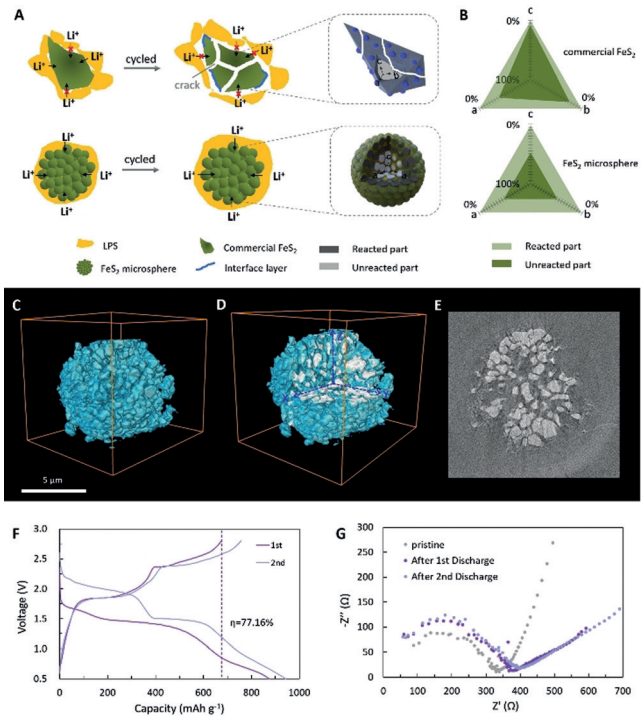

Figure 6. In situ growth in the solid-state sulfide electrolyte. A) The process of Li insertion in commercial FeS_2 and porous FeS_2 microsphere electrodes. B) Comparison of reaction depth and reaction uniformity of active materials along with *a*, *b*, and *c* axes. C)–E) The 3D view and cut-view of the porous FeS_2 microsphere. F) Galvanostatic charge–discharge profiles of FeS_2@$Li_7P_3S_{11}$ nanocomposites. G) Impedance spectra showing lower and relatively stable resistance of the improved solid-state cell over cycles.

In Situ Growth in the Solid-State Sulfide Electrolyte

Our finding directly links electrode–electrolyte interface behaviors and capacity fading phenomena that are directly associated with the solid-state battery electrochemistry. An illustration (Figure 6A) interprets the phase evolution of FeS_2 in solid-state lithium batteries. First, the heterogeneous phase conversion dominates the conversion reactions, which may directly affect battery electrochemical performance. The heterogeneous phase transformation is likely caused in part by the unidirectional propagation pathway at solid–solid interfaces. In general, particles with different morphologies and edges may form inhomogeneous contact with the solid-state electrolyte, resulting in different conversion rates and inhomogeneous electrochemical reactions at 3D (Figure 6B). Our operando synchrotron X-ray nanotomography clearly shows multiple propagation fronts proceed inhomogeneously at the FeS_2 particles. Second, the contact loss between the solid-state electrolyte and active FeS_2 particles and meanwhile the absence of ion conductive pathways may be also responsible for the low coulombic efficiency and capacity fading of the solid-state battery. With SEM images and impedance spectroscopy at different DODs, it was found that there were some cracks appeared in the FeS_2 particles, which originate from the large volume expansion of FeS_2 during the discharging periods. Furthermore, the surface accumulation of Fe phase and formation of the dense surface metallic layer may also block the ionic transport, increase the diffusion path in which both ions and electrons reach simultaneously, which affect the electrochemical kinetics for solid-state batteries, as shown in a sphere model of Figure 6A.

The above results infer that the low electrochemical performance in solid-state batteries is largely attributed to the electrochemically induced ionic/electronic contact loss in the solid–solid interface. Presumably, the driving force associated with the contact loss originates from large volume expansion and heterogeneous phase transformation during the initial lithium-ion insertion process. Therefore, to minimize this unwanted chemo-mechanical effect, an ideal solution is to develop a synergy strategy by designing the active battery particles with the porous structure to buffer volume change and simultaneously fabricating a robust solid–solid electrolyte interface to self-heal the continuous contact loss. To verify our assumption, we synthesized porous FeS_2 microsphere with second particles and in situ growth in the solid-state sulfide electrolyte within the FeS_2 microspheres. The 3D view and cut-view of FeS_2 microsphere are shown in Figure 6C–E. Owing to the in situ growth and strong bond, the FeS_2 particles are embedded well in the solid electrolyte, which provides a 3D ionic conductive network, as shown in Figure 6F. The advantage of the strategy is verified by good preservation of the interfacial contact between battery active particles and solid-state electrolyte after lithiation–delithiation.[24] We therefore propose this optimized microstructural and interfacial design to reduce the contact loss owing to the stress and volume changes of the battery materials (Figure 6G), which relieve electrochemical–mechanical induced capacity fading and improve solid-state battery performance (Supporting Information, Figure S12).

Conclusion

In summary, the chemomechanical interplay evolution of the FeS_2 electrode in solid-state batteries was investigated by a combination of operando synchrotron X-ray nanotomography with electron microscopy. The high irreversible capacity in solid-state batteries originated from multi-factors, including chemomechanical effect, heterogeneous phase transformation and the augmentation of metallic surface passivation layers. Here, for the first time, we provide direct visualized evidence that the heterogeneous phase transformation and internal strain-induced contact loss limit electrochemical reaction in conversion electrodes. The accumulation of surface metallic phase upon lithiation also builds up the obstacle for lithium-ion transport. With in situ growth of solid sulfide electrolyte into a 3D FeS_2 microstructure, these chemomechanical and interfacial issues can be significantly inhibited and superior electrochemical performance can be achieved. Our study provides new insights into phase conversion in solid-state batteries and sheds light on the solid–solid interfacial issues in solid battery electrodes.

Acknowledgements

This work was supported by HIT "Young Scientist Studio" and the Start-up Funds from Harbin Institute of Technology, Natural Science Foundation of Heilongjiang Province (No. ZD2019B001), HIT Research Institute (Zhao Yuan) of New Materials and Intelligent Equipment Technology Co., Ltd. Scientific and Technological Cooperation and Development Fund (No.2017KJHZ002). This research used resources at FXI beamline (18-ID) of the National Synchrotron Light Source-II, a U.S. Department of Energy (DOE) Office of Science User Facility operated for the DOE Office of Science by Brookhaven National Laboratory under Contract No. DE-SC0012704.

Conflict of interest

The authors declare no conflict of interest.

Keywords: electrochemistry · interfaces · lithium · solid-state batteries · sulfide electrolyte

How to cite: *Angew. Chem. Int. Ed.* **2019**, *58*, 18647–18653
Angew. Chem. **2019**, *131*, 18820–18826

[1] a) S. Chu, Y. Cui, N. Liu, *Nat. Mater.* **2017**, *16*, 16–22; b) Y. Shao, J. P. Dodelet, G. Wu, P. Zelenay, *Adv. Mater.* **2019**, *31*, 1807615; c) V. Chabot, D. Higgins, A. Yu, X. Xiao, Z. Chen, J. Zhang, *Energy Environ. Sci.* **2014**, *7*, 1564–1596; d) F. Wu, S. Chen, V. Srot, Y. Huang, S. K. Sinha, P. A. van Aken, J. Maier, Y. Yu, *Adv. Mater.* **2018**, *30*, 1706643; e) M. Li, J. Lu, Z. Chen, K. Amine, *Adv. Mater.* **2018**, *30*, 1800561; f) Y. Li, Q. Li, H. Wang, L. Zhang, D. P. Wilkinson, J. Zhang, *Electrochem. Energy Rev.* **2019**, https://doi.org/10.1007/s41918-019-00052-4; g) R. Quintero-Bermudez, A. Gold-Parker, A. H. Proppe, R. Munir, Z. Yang, S. O. Kelley, A. Amassian, M. F. Toney, E. H. Sargent, *Nat. Mater.* **2018**, *17*, 900–907; h) F. Lin, Y. Liu, X. Yu, L. Cheng, A. Singer, O. G. Shpyrko, H. L. Xin, N. Tamura, C. Tian, T. C. Weng, X. Q. Yang, Y. S. Meng, D. Nordlund, W. Yang, M. M. Doeff, *Chem. Rev.* **2017**, *117*, 13123–13186; i) Y. Ding, Z. P. Cano, A. Yu, J. Lu, Z. Chen, *Electrochem. Energy Rev.* **2019**, *2*, 1–28; j) J. Hong, W. E. Gent, P. Xiao, K. Lim, D. H. Seo, J. Wu, P. M. Csernica, C. J. Takacs, D. Nordlund, C. J. Sun, K. H. Stone, D. Passarello, W. Yang, D. Prendergast, G. Ceder, M. F. Toney, W. C. Chueh, *Nat. Mater.* **2019**, *18*, 256–265; k) X. Chen, T. Hou, K. A. Persson, Q. Zhang, *Mater. Today* **2019**, *22*, 142–158; l) X. Li, J. Liang, X. Li, C. Wang, J. Luo, R. Li, X. Sun, *Energy Environ. Sci.* **2018**, *11*, 2828–2832.

[2] Y. Kato, S. Hori, T. Saito, K. Suzuki, M. Hirayama, A. Mitsui, M. Yonemura, H. Iba, R. Kanno, *Nat. Energy* **2016**, *1*, 16030.

[3] a) Z. Gao, H. Sun, L. Fu, F. Ye, Y. Zhang, W. Luo, Y. Huang, *Adv. Mater.* **2018**, *30*, 1705702; b) C. Sun, J. Liu, Y. Gong, D. P. Wilkinson, J. Zhang, *Nano Energy* **2017**, *33*, 363–386; c) E. Umeshbabu, B. Zheng, Y. Yang, *Electrochem. Energy Rev.* **2019**, *2*, 199–230.

[4] A. Manthiram, X. Yu, S. Wang, *Nat. Rev. Mater.* **2017**, *2*, 16103.

[5] N. Kamaya, K. Homma, Y. Yamakawa, M. Hirayama, R. Kanno, M. Yonemura, T. Kamiyama, Y. Kato, S. Hama, K. Kawamoto, A. Mitsui, *Nat. Mater.* **2011**, *10*, 682–686.

[6] a) W. Hou, X. Guo, X. Shen, K. Amine, H. Yu, J. Lu, *Nano Energy* **2018**, *52*, 279–291; b) K. H. Park, Q. Bai, D. H. Kim, D. Y. Oh, Y. Zhu, Y. Mo, Y. S. Jung, *Adv. Energy Mater.* **2018**, *8*, 1800035.

[7] a) D. Santhanagopalan, D. Qian, T. McGilvray, Z. Wang, F. Wang, F. Camino, J. Graetz, N. Dudney, Y. S. Meng, *J. Phys. Chem. Lett.* **2014**, *5*, 298–303; b) R. Koerver, I. Aygün, T. Leichtweiß, C. Dietrich, W. Zhang, J. O. Binder, P. Hartmann, W. G. Zeier, J. Janek, *Chem. Mater.* **2017**, *29*, 5574–5582.

[8] a) A. O. Kondrakov, A. Schmidt, J. Xu, H. Geßwein, R. Mönig, P. Hartmann, H. Sommer, T. Brezesinski, J. Janek, *J. Phys. Chem. C* **2017**, *121*, 3286–3294; b) R. Koerver, W. Zhang, L. de Biasi, S. Schweidler, A. O. Kondrakov, S. Kolling, T. Brezesinski, P. Hartmann, W. G. Zeier, J. Janek, *Energy Environ. Sci.* **2018**, *11*, 2142–2158; c) W. Zhang, D. Schröder, T. Arlt, I. Manke, R. Koerver, R. Pinedo, D. A. Weber, J. Sann, W. G. Zeier, J. Janek, *J. Mater. Chem. A* **2017**, *5*, 9929–9936.

[9] Y. Zhu, X. He, Y. Mo, *J. Mater. Chem. A* **2016**, *4*, 3253–3266.

[10] S. P. Culver, R. Koerver, W. G. Zeier, J. Janek, *Adv. Energy Mater.* **2019**, *9*, 1900626.

[11] Q. Zhang, J. P. Mwizerwa, H. Wan, L. Cai, X. Xu, X. Yao, *J. Mater. Chem. A* **2017**, *5*, 23919–23925.

[12] S. Wenzel, D. A. Weber, T. Leichtweiss, M. R. Busche, J. Sann, J. Janek, *Solid State Ionics* **2016**, *286*, 24–33.

[13] T. A. Yersak, H. A. Macpherson, S. C. Kim, V.-D. Le, C. S. Kang, S.-B. Son, Y.-H. Kim, J. E. Trevey, K. H. Oh, C. Stoldt, S.-H. Lee, *Adv. Energy Mater.* **2013**, *3*, 120–127.

[14] X. Yao, D. Liu, C. Wang, P. Long, G. Peng, Y. S. Hu, H. Li, L. Chen, X. Xu, *Nano Lett.* **2016**, *16*, 7148–7154.

[15] M. R. Busche, D. A. Weber, Y. Schneider, C. Dietrich, S. Wenzel, T. Leichtweiss, D. Schröder, W. Zhang, H. Weigand, D. Walter, S. J. Sedlmaier, D. Houtarde, L. F. Nazar, J. Janek, *Chem. Mater.* **2016**, *28*, 6152–6165.

[16] F. Mizuno, A. Hayashi, K. Tadanaga, M. Tatsumisago, *Adv. Mater.* **2005**, *17*, 918–921.

[17] a) D. Y. Wang, C. H. Li, S. S. Li, T. R. Kuo, C. M. Tsai, T. R. Chen, Y. C. Wang, C. W. Chen, C. C. Chen, *Sci. Rep.* **2016**, *6*, 20397; b) B. Mao, Q. Dong, C. L. Exstrom, J. Huang, *Thin Solid Films* **2014**, *562*, 361–366.

[18] H. Xue, D. Y. W. Yu, J. Qing, X. Yang, J. Xu, Z. Li, M. Sun, W. Kang, Y. Tang, C.-S. Lee, *J. Mater. Chem. A* **2015**, *3*, 7945–7949.

[19] a) D. S. Coburn, E. Nazaretski, W. Xu, M. Ge, C. Longo, H. Xu, K. Gofron, Z. Yin, H. H. Chen, Y. Hwu, W.-K. Lee, *Rev. Sci. Instrum.* **2019**, *90*, 053701; b) M. Ge, D. S. Coburn, E. Nazaretski, W. Xu, K. Gofron, H. Xu, Z. Yin, W.-K. Lee, *Appl. Phys. Lett.* **2018**, *113*, 083109.
[20] J. Wang, Y. C. Chen-Wiegart, J. Wang, *Angew. Chem. Int. Ed.* **2014**, *53*, 4460 – 4464; *Angew. Chem.* **2014**, *126*, 4549 – 4553.
[21] F. Lin, D. Nordlund, T. C. Weng, Y. Zhu, C. Ban, R. M. Richards, H. L. Xin, *Nat. Commun.* **2014**, *5*, 3358.
[22] Y. Xu, E. Hu, K. Zhang, X. Wang, V. Borzenets, Z. Sun, P. Pianetta, X. Yu, Y. Liu, X.-Q. Yang, H. Li, *ACS Energy Lett.* **2017**, *2*, 1240 – 1245.
[23] F. Hao, X. Chi, Y. Liang, Y. Zhang, R. Xu, H. Guo, T. Terlier, H. Dong, K. Zhao, J. Lou, Y. Yao, *Joule* **2019**, *3*, 1349 – 1359.
[24] H. Wan, J. P. Mwizerwa, X. Qi, X. Liu, X. Xu, H. Li, Y. S. Hu, X. Yao, *ACS Nano* **2018**, *12*, 2809 – 2817.

Manuscript received: August 28, 2019
Accepted manuscript online: October 14, 2019
Version of record online: November 6, 2019

